STELLAR POPULATIONS OF Lyα EMITTERS AT $z = 4.86$: A COMPARISON TO $z \sim 5$ LYMAN BREAK GALAXIES[*]

Suraphong Yuma[1], Kouji Ohta[1], Kiyoto Yabe[1], Kazuhiro Shimasaku[2], Makiko Yoshida[2], Masami Ouchi[3], Ikuru Iwata[4], and Marcin Sawicki[5]

[1] Department of Astronomy, Kyoto University, Sakyo-ku, Kyoto 606-8502, Japan; yuma@kusastro.kyoto-u.ac.jp
[2] Department of Astronomy, School of Science, University of Tokyo, Tokyo 113-0033, Japan
[3] Observatories of the Carnegie Institution of Washington, 813 Santa Barbara Street, Pasadena, CA 91101, USA
[4] Okayama Astrophysical Observatory, National Astronomical Observatory of Japan, Okayama 719-0232, Japan
[5] Department of Astronomy and Physics, Saint Mary's University, 923 Robie Street, Halifax, Nova Scotia, B3H 3C3, Canada

ABSTRACT

We present a study of a stellar population of Lyα emitters (LAEs) at $z = 4.86$ in the Great Observatories Origins Deep Survey North (GOODS-N) field and its flanking field. The LAEs are selected based on optical narrowband (NB711) and broadband (V, I_c, and z') observations by the Suprime-Cam attached to the Subaru Telescope. With the publicly available Infrared Array Camera (IRAC) data in GOODS-N and further IRAC observations in the flanking fields, we select five LAEs that are not contaminated by neighboring objects in IRAC images and construct their observed spectral energy distributions (SEDs) with I_c, z', IRAC 3.6 μm, and 4.5 μm band photometries. The SEDs cover the rest-frame UV-to-optical wavelengths. We derive the stellar masses, ages, color excesses, and star formation rates (SFRs) of the five LAEs using an SED fitting method. Assuming a constant star formation history, we find that the stellar masses range from 10^8 to 10^{10} $M_\odot$ with the median value of 2.5×10^9 $M_\odot$. The derived ages range from very young (7.4 Myr) to 437 Myr, with a median age of 25 Myr. The color excess $E(B - V)$ is between 0.1 and 0.4 mag. SFRs are 55–209 $M_\odot$ yr^{-1}. A comparison of the stellar populations is made between 3 LAEs and 88 Lyman break galaxies (LBGs) selected at the same redshift, in the same observed field, and down to the same limit of the rest-frame UV luminosity. These three LAEs are the brightest and reddest samples of all the LAE samples at $z = 4.86$. The LAEs are distributed at the relatively faint part of the UV-luminosity distribution of LBGs. Deriving the stellar properties of the LBGs by fitting their SEDs with the same model ensures that model difference does not affect the comparison. It is found that the stellar properties of the LAEs are located in the region where the properties of LBGs are distributed. On average, the LAEs show less dust extinction and lower SFRs than LBGs, while the stellar mass of LAEs lies nearly in the middle part of the mass distribution of LBGs. However, the stellar properties of LAEs and LBGs are similar at the fixed UV or optical luminosity. We also examine the relations between the output properties from the SED fitting and the rest-frame Lyα equivalent width, but cannot find any significant correlation.

Key words: galaxies: evolution – galaxies: formation – galaxies: high-redshift

Online-only material: color figures

1. INTRODUCTION

There are two popular techniques for isolating galaxies at high redshift ($z \gtrsim 3$): broadband selection (i.e., Lyman break technique) and narrowband selection. Lyman break galaxies (LBGs) are selected by the Lyman break technique by taking advantage of the spectral discontinuity due to the neutral hydrogen attenuation in the intergalactic medium (IGM) at rest-frame wavelengths shorter than 912/1216 Å. By using this method, a large number of high-redshift galaxies are studied (e.g., Steidel et al. 1996, 1999, 2003; Giavalisco et al. 1996, 1998; Lowenthal et al. 1997; Pettini et al. 1998; Shapley et al. 2001, 2003; Iwata et al. 2003, 2007; Papovich et al. 2004; Bouwens et al. 2004, 2008; Reddy et al. 2005, 2006, 2008; Sawicki & Thompson 2005, 2006; Yoshida et al. 2006). The other method is to select galaxies with strong Lyα emission lines which fall into a narrowband filter. This method is useful for selecting high-redshift galaxies that have a strong Lyα emission line. These objects are called Lyα emitters (LAEs). Partridge & Peebles (1967) proposed that primordial galaxies in the early stage of their formation should show a strong Lyα emission line. LAEs are thus expected to be young galaxies with low metallicity. Many surveys have been undertaken to search for galaxies with a strong Lyα emission at various redshifts ranging from 2.1 to 6.6 or even more (e.g., Hu & McMahon 1996; Cowie & Hu 1998; Hu et al. 1998, 2004; Rhoads et al. 2000, 2004; Kudritzki et al. 2000; Rhoads & Malhotra 2001; Malhotra & Rhoads 2002; Fynbo et al. 2001; Ouchi et al. 2003, 2008; Fujita et al. 2003; Shimasaku et al. 2003, 2004, 2006; Kodaira et al. 2003; Ajiki et al. 2003, 2004, 2006; Taniguchi et al. 2005; Venemans et al. 2002, 2004; Iye et al. 2006; Ota et al. 2008; Nilsson et al. 2009; Guaita et al. 2010).

In order to examine the evolutionary stage of LAEs and to reveal what kind of galaxiers they are, various properties of LAEs have been studied such as luminosity functions (e.g., Ouchi et al. 2003, 2008; Malhotra & Rhoads 2004; Shimasaku et al. 2006; Kashikawa et al. 2006; Gronwall et al. 2007; Ota et al. 2008) and clustering properties (e.g., Ouchi et al. 2003; Shimasaku et al. 2003, 2004, 2006; Kashikawa et al. 2006; Murayama et al. 2007). Revealing the stellar population of LAEs is crucial for understanding their physical nature. In order to do that, the spectral energy distribution (SED) of a galaxy is compared with stellar population synthesis models produced by varying the ages, metallicities, amounts of dust extinctions,
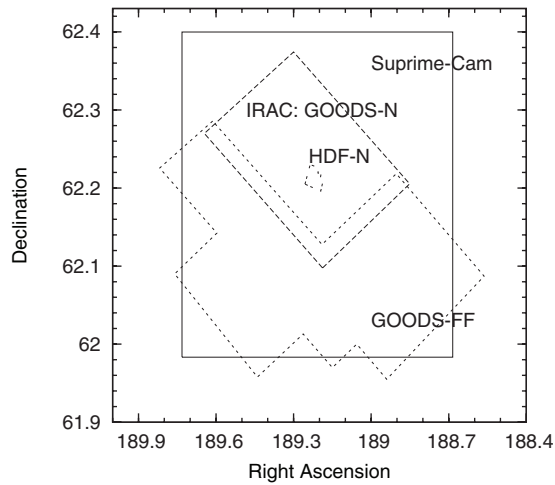

Figure 1. Observed fields. The solid line indicates the effective field observed with Suprime-Cam, while the long and short dashed lines show the GOODS-N and GOODS-FF fields observed with IRAC. HDF-N is shown as a reference at the center of the figure.

Figure 2. Transmission curves of V, NB711, I_c, and z' bandpasses. CCD response, transmission of PFC, mirror reflectivity, and airmass (sec $z = 1.2$) are included. Also shown is a model spectrum in the unit of μJy (solid line) of a star-forming galaxy at $z = 4.86$ including a Lyα emission line with an EW$_{\rm rest}$ of 10 Å. The model is constructed using the Bruzual & Charlot (2003) stellar synthesis code. A constant star formation history and Salpeter IMF are assumed at an age of 12 Myr and at the SFR of 1 $M_\odot$ yr^{-1}. The attenuation by IGM is applied using the prescription by Madau (1995).

star formation rates (SFRs), etc. The stellar population of a galaxy can be constrained from the best-fit model. This method is known as the SED fitting method. Recent studies show that LAEs have wide ranges of ages (1 Myr to 1 Gyr) and stellar masses (10^6–10^{10} $M_\odot$; e.g., Gawiser et al. 2006, 2007; Lai et al. 2007, 2008; Nilsson et al. 2007; Finkelstein et al. 2007, 2008, 2009; Pirzkal et al. 2007). Among these studies, stacking analysis shows that LAEs at $z \sim 3$ are free from dust or show modest dust extinction ($E(B - V) \leqslant 0.03$ mag; e.g., Gawiser et al. 2006, 2007; Lai et al. 2008; Ono et al. 2010), whereas SED fitting of an individual LAE at higher redshifts suggests that some of the LAEs show significant dust extinction (e.g., Lai et al. 2007; Finkelstein et al. 2009).

It is important to investigate the connection between LAEs and other galaxy populations selected by different methods, i.e., LBGs that are selected based on UV continuum. Since these two methods suffer from different biases, the selected galaxies partially overlap and the relationship between them is not clear. Shapley et al. (2001) divided LBGs at $z \sim 3$ into two subsamples according to their ages obtained by SED fitting: an "old subsample" with ages about 1 Gyr and a "young subsample" with ages less than 35 Myr. They found that the old subsample shows a strong Lyα emission line, while the young subsample does not. In other words, they found that LBGs with a Lyα emission line are older than those without a Lyα emission line. Confirming this statement, the recent work with a larger sample at the same redshift by Kornei et al. (2010) shows that objects with rest-frame Lyα equivalent width (EW) larger than 20 Å seem to be older, lower in SFR, and less dusty than those without a Lyα emission line. Pentericci et al. (2007), in contrast, found that at $z \sim 4$ LBGs with Lyα emission are less massive and younger than those with no line. Considering the results from the SED analysis mentioned above, there may be an evolution of differences between LAEs and LBGs with redshifts (e.g., Shimizu & Umemura 2010). Although there are some SED studies at higher redshift ($z \gtrsim 5$; Pirzkal et al. 2007; Lai et al. 2007), the relationship between LAEs and LBGs is still unknown. In this paper, we study the stellar populations of LAEs at $z = 4.86$ from their rest-frame UV-to-optical SEDs. Down to the same UV luminosity, the derived stellar properties of LAEs are compared to those of LBGs by Yabe et al. (2009).
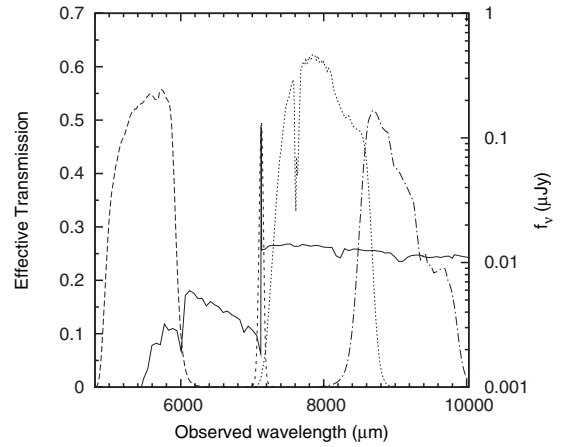
They selected LBGs at the same redshift range in the same field and used the same fitting code and synthesis spectral model assumptions. This direct comparison between LAEs and LBGs is expected to reveal their differences and to help define the kind of properties that make a galaxy an LAE.

Data sources and photometry are described in Section 2. Section 3 explains the selection criteria and the LAE candidates. The observed SEDs are constructed for each LAE candidate and compared to the models in Section 5. The fitting results are shown in Section 6. Section 7 offers comparisons between LAEs and LBGs. The summary is given in Section 8. Throughout this paper, we use the AB magnitude system (Oke & Gunn 1983) and adopt a cosmology with parameters of $\Omega_{\rm m} = 0.3$, $\Omega_\Lambda = 0.7$, and $H_0 = 70$ km s^{-1} Mpc^{-1}.

2. DATA SOURCES AND PHOTOMETRY

2.1. Optical Data

2.1.1. Observations and Data Reduction

Optical data were obtained with the Suprime-Cam (Miyazaki et al. 2002) attached to the Subaru Telescope (Iye et al. 2004). The observed field is toward the Hubble Deep Field-North (HDF-N; Williams et al. 1996) [R.A.(2000) = $12^{\rm h}36^{\rm m}49^{\rm s}.4$, decl.(2000) = $+62°12'58''$] and is illustrated by the solid line in Figure 1. The pixel scale of the CCD was $0''.20$. We used NB711 ($\lambda_{\rm eff} = 7126$ Å, FWHM $= 73$ Å) and three broadband filters, V, I_c, and z', to select $z = 4.86$ LAEs. The effective redshift interval calculated from the FWHM of NB711 is $4.83 \leqslant z \leqslant 4.89$. Transmission curves, which include the responses of CCD, prime focus corrector (PFC), mirror, and airmass of all filters used in this work are shown in Figure 2. The observation with the NB711 filter was made on 2005 March 16. Images were taken with a dithering of $\sim 80''$ and an exposure time of 1200 s for each frame. With 23 exposures, we covered a ~ 750 arcmin^2 field of view. The total integration time was 7.7 hr. The weather condition was not so excellent. Seeing size during the observation was $1''.5$ on average.

Data reduction was made by using SDFRED version 1.4.1, the software developed for Suprime-Cam data reduction (Yagi

et al. 2002; Ouchi et al. 2004). After bias subtraction, flat fielding, and distortion correction, image mosaicking was made by identifying 30–170 non-saturated stars common in several object frames. The frame alignment and correction for flux/count and FWHM were made based on these star data. The resulting FWHM of point sources in the mosaicked image is $\sim$1$''$7.

Astrometry was performed based on the USNO-A2 catalog by fitting with the third-order polynomial coefficients to $\sim$1000 stars identified in the mosaicked image. The positional error is about 0$''$2 rms over the image. The magnitude zero point was derived based on the imaging data of two spectrophotometric standard stars (G191-B2B and HZ44) taken during the same observing night. As an independent check for photometry in NB711 images, we derived NB711 magnitudes of stars by interpolating their V, I_c, and z' magnitudes. The derived magnitude zero points are in agreement within $\sim$0.18 mag. A 3σ limiting magnitude at 2$''$5 diameter aperture is 26.16 mag for the NB711 image.

The observations and data reductions of broadband images are described in detail by Iwata et al. (2007). The images were taken with V, I_c, and z' filters in 2001 February. The typical seeing during the observations was $\sim$1$''$1. In addition, Iwata et al. (2007) also used the imaging data taken from 2001 February to April by the University of Hawaii (UH) group (Capak et al. 2004), who used the same instrument and filters. The final effective survey area is 508.5 arcmin^2. The limiting magnitudes of V-, I_c-, and z'-band images are 28.1, 26.8, and 26.6 mag, respectively (3σ at 1$''$6 diameter aperture). The broadband images were all degraded to a point-spread function (PSF) size of 1$''$7 to match that of the NB711 image. The 3σ limiting magnitudes of the final PSF matched images at 2$''$5 diameter aperture are 27.3, 26.1, and 25.9 mag for V, I_c, and z' images, respectively.

2.1.2. Photometric Catalog

The photometric catalogs of the optical images were made by using SExtractor version 2.5.2 (Bertin & Arnouts 1996). The positions of objects were extracted from the NB711 image and the photometry was then made at the extracted positions in all optical images via dual-image mode. In order to use the dual-image mode, we first had to make a position registration between the broadband images and the NB711 image. Position mapping between the images was made by using *geomap* in IRAF[6] based on positions of the bright but non-saturated stars detected in the images. The registration of the images was performed by *gregister*. The accuracy in making a position registration is within 0.2 pixels or 0$''$04 rms. After image registration, we subtracted GLOBAL background from each registered image individually[7] and homogenized the broadband images so that they all have the same seeing size as the NB711 image within 0$''$01 accuracy by *gauss*. The dual-image mode was then performed, using the following parameters. The images were filtered with a default convolution kernel (default.conv). The LOCAL background was estimated using a 64 × 64 pixel background mesh with 3 × 3 median filtering. An object was detected with a minimum of five connected pixels above a 2.0σ minimum threshold. These parameters are found

to maximize the number of detected objects in the NB711 image and minimize the detected numbers of objects in the negative NB711 images.

In the SED fitting process, the total photometry of the objects is necessary. The total magnitudes were obtained by applying aperture corrections to 2$''$5 diameter aperture magnitudes. We examined the aperture sizes to determine the best value and chose 2$''$5, which maximizes the signal-to-noise ratio (S/N). The aperture corrections were determined from the Monte Carlo simulations where artificial objects with PSF shapes corresponding to the seeing size of 1$''$7 were put into the original image and then detected by using the same SExtractor parameters. In the simulations, our objects were implicitly assumed to be point sources since their apparent size in the image is comparable to that of the PSF. The PSF was made by stacking images of the PSF that shows the stellarity index larger than 0.98 and has no nearby objects. The aperture correction factors are -0.30 ± 0.01 and -0.33 ± 0.01 mag for I_c and z' images, respectively, where the errors are the PSF uncertainties. Errors of the total magnitudes are the combination of the 1σ error in the photometry of simulated objects and the uncertainties of correction factors. Because we do not use V and NB711 images in the SED fitting process, we do not compute the aperture corrections for them.

2.2. Mid-infrared Data

Mid-infrared images are obtained from deep observations with the Infrared Array Camera (IRAC) on the *Spitzer Space Telescope*. We used the publicly available mid-infrared data in the Great Observatories Origins Deep Survey North (GOODS-N; Dickinson et al. 2003) field centered at 12^{h}36^{m}54^{s}87, +62$°$14$'$19$''$2 (J2000) provided by the *Spitzer Space Telescope* Legacy Science program.[8] The field covers an area of approximately 10$'$ × 16$'$ or $\sim$160 arcmin^2 as shown in Figure 1. In this work, we used the First Data Release (DR1) and Second Data Release (DR2) of IRAC data consisting of imaging data in 3.6, 4.5, 5.8, and 8.0 μm bandpasses. The pixel scale of all images after being drizzled is 0$''$60 pixel^{-1}. The mean FWHM of the PSF in IRAC GOODS-N images is $\sim$1$''$7. The 3σ limiting magnitudes of IRAC 3.6, 4.5, 5.8, and 8.0 μm images at 2$''$4 diameter aperture are 25.9, 25.8, 23.7, and 23.6 mag, respectively.

In addition to the very deep GOODS-N data, data in the flanking field (hereafter GOODS-FF) of GOODS-N are obtained to cover a part of the Subaru observation area. The GOODS-FF observations were carried out with the IRAC in 2005 December and 2006 June (the *Spitzer* GO program (GO-20218); PI: Ikuru Iwata). The observations were made by pointing at five different positions on the sky around the GOODS-N field. The total exposure time for each passband is 4000 s. Basic Calibrated Data (BCD) processed by the pipeline of the Spitzer Science Center (SSC) were used. The images were drizzled using MOPEX software provided by SSC and combined together to get an improved mosaic image covering the whole observed area of $\sim$300 arcmin^2. The mosaic image has a final pixel scale of 0$''$61 pixel^{-1} and a PSF size (FWHM) of 1$''$7. The 3σ magnitude limits at 2$''$4 diameter aperture are 25.0, 24.6, 22.1, and 22.3 for IRAC 3.6, 4.5, 5.8, and 8.0 μm bands, respectively. Combining the infrared data obtained in the GOODS-N and GOODS-FF fields, we have the effective area of $\sim$400 arcmin^2 covering $\sim$80% of Subaru images as seen in Figure 1.

---

[6] IRAF is distributed by the National Optical Astronomy Observatory, which is operated by the Association of Universities for Research in Astronomy, Inc., under cooperative agreement with the National Science Foundation.

[7] Based on our simulation with artificial objects, the processes of subtracting the background before smoothing the images and re-subtracting the LOCAL background in SExtractor give better photometry.

[8] http://ssc.spitzer.caltech.edu/spitzermission/observingprograms/legacy/goods/

The photometry of IRAC was done based on the positions of the LAEs at $z = 4.86$, which are selected from the criteria described in the following section. Since the dimensions and the pixel scale of the narrowband image and IRAC images are different, we could not use the dual-image mode in SExtractor to determine the aperture photometry in IRAC images. *Phot* provided by IRAF was used instead to perform aperture photometry at $2''.4$ diameter, which we determined to be the best aperture size since it maximizes the S/N. Because the positions in the NB711 image are used as the reference, we made a registration of the IRAC images before performing IRAC photometry of the objects. The position alignment was made globally for each IRAC image by using positions of point sources detected in both NB711 and IRAC images. The estimated errors in determining the position shifts are $0''.1$ (0.17 pixels) for IRAC images in the GOODS-N field and $0''.2$ (0.33 pixels) for those in the GOODS-FF. Since the error of $0''.2$ may not be negligible, we re-did the photometry of objects at the positions separated from the corrected positions by $0''.2$ and found the magnitude difference to be less than 0.2 mag. This magnitude difference gives less than 3% difference in the stellar masses derived from SED fitting.

Aperture corrections for IRAC images were determined by the following process. The artificial objects with IRAC PSF are put into the IRAC images. The PSF was made from images of objects identified to be a stellar object in Subaru images. For the GOODS-N field, the correction factors are -0.62 mag and -0.72 mag in the $3.6\,\mu$m and $4.5\,\mu$m bands, respectively. The correction uncertainties due to the uncertainties in PSFs are 5% and 6% in the $3.6\,\mu$m and $4.5\,\mu$m bands, respectively. For GOODS-FF images, they are, respectively, -0.70 mag and -0.73 mag with 6% and 7% uncertainties in the $3.6\,\mu$m and $4.5\,\mu$m bands. Errors in IRAC photometry are 1σ standard deviations of sky background and the uncertainties of correction factors. Since $5.8\,\mu$m and $8.0\,\mu$m images show too low S/N to place a useful upper limit in the SED fitting process, we do not use them in our further analysis.

3. SAMPLE SELECTION

A total of 29,675 objects were detected with NB711 < 26.0 mag (3.5σ limiting magnitude). Figure 3 shows the I_c − NB711 color versus NB711 magnitudes of all objects (black dots). We selected NB711-excess objects from the following selection criteria:

$$I_c - \text{NB711} > 0.64 \qquad (1)$$

and

$$I_c - \text{NB711} > 3\sigma_{I_c - \text{NB711}}, \qquad (2)$$

where $3\sigma_{I_c - \text{NB711}}$ is a 3σ error in measuring I_c − NB711 color for a source with a color of I_c − NB711 $= -0.28$ mag, the average color of all objects with NB711 magnitudes brighter than 26.0 mag. Note that the magnitudes and colors of objects used in the sample selection are the values at the $2''.5$ diameter aperture, except for those noted otherwise. The first criterion corresponds to a rest-frame equivalent width (EW_{rest}) of 10 Å assuming a flat continuum ($f_\nu = $ constant). The EW cut of 10 Å used in this paper is lower than that commonly used in other LAE studies (20 Å). Other studies (e.g., Ouchi et al. 2003; Nilsson et al. 2009) compute the EW by using the average continuum flux density from the continuum both blueward and redward of the Lyα line, while the continuum in this work is extrapolated from the continuum redward of the Lyα line. Because the blueward
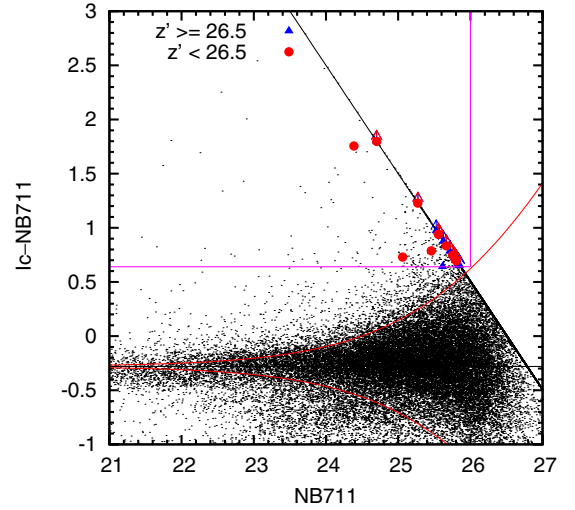

Figure 3. I_c − NB711 color vs. NB711 $2''.5$ aperture magnitude. LAEs with $z'_{\text{total}} < 26.5$ mag are shown with filled circles; filled triangles represent those with $z'_{\text{total}} \geqslant 26.5$ mag. Arrows show the lower limits of I_c − NB711 taken at 2σ I_c limiting magnitude. Note that we used 2σ I_c limiting magnitude as a lower limit for objects whose I_c magnitudes are fainter than that. A diagonal black line indicates 2σ limiting magnitude of the I_c image. Red curves indicate the distributions of 3σ errors in measuring I_c − NB711 color for a source with a color of I_c − NB711 $= -0.28$ mag, the average color of all objects brighter than NB711 $= 26.0$ mag. The horizontal and vertical magenta lines show the NB711-excess criterion and NB711 $= 26.0$ mag limit, respectively.

(A color version of this figure is available in the online journal.)

continuum suffers from the attenuation by neutral hydrogen in the IGM at high redshift, the continuum estimated by the latter method is expected to be higher than that in the usual case. Consequently, the EW computed in this paper is smaller than that from other studies, even though the object has the same redward continuum. The Lyα EWs computed in the usual way are also shown in Table 2; most of the LAEs compared to LBGs show the EWs larger than 20 Å when we adopt the commonly used method.

By the above criteria, 667 objects were selected. Among them, there are low-redshift interlopers with strong emission lines such as Hα, Hβ, [O III]λ5007, or [O II]λ3727. To rule them out, we first divided the objects selected by the above criteria into two groups according to their brightness in the z' band. For candidates with $z'_{\text{total}} < 26.5$ mag, we adopted the following criteria, which were used by Iwata et al. (2007, see their Figure 2) to select LBGs at $z \sim 5$:

$$z'_{\text{total}} < 26.5, \qquad (3)$$

$$V - I_c > 1.55, \qquad (4)$$

and

$$V - I_c > 7.0(I_c - z') + 0.15, \qquad (5)$$

where z'_{total} is the total magnitude in the z' band and the colors are derived from $2''.5$ diameter aperture magnitudes. These criteria have been confirmed by spectroscopic follow-up observations (Ando et al. 2004, 2007; Kajino et al. 2009). For objects with $z'_{\text{total}} \geqslant 26.5$ mag, we required non-detection in the V-band magnitude ($V > 1\sigma$ limiting magnitude). As a result, 24 objects meet all criteria simultaneously down to NB711 $= 26.0$ mag as illustrated in Figure 3. Eleven of them show z' magnitudes brighter than 26.5 mag. Note that z'_{total} here is slightly different from z'_{magauto} by Iwata et al. (2007; up to
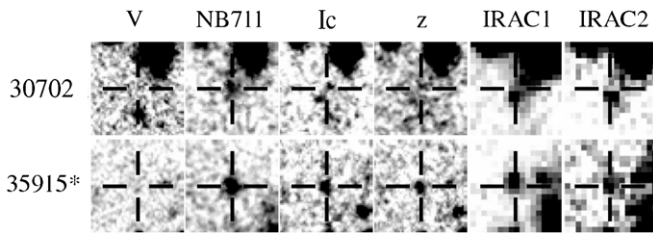
Figure 4. Montage of images of group I LAEs. Size of each image is $10'' \times 10''$ with an LAE at the center of the image. North is at the top; east is to the left. IDs of objects are shown on the left of the figure. Note that the Subaru broadband images displayed here (V, I_c, and z') are those before smoothing. An asterisk indicates the LAE with the spectroscopic redshift.
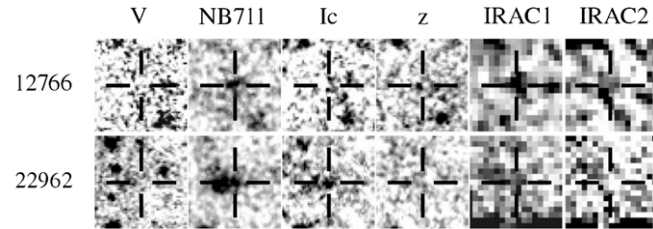

Figure 5. Same as Figure 4 but for group II LAEs.

± 0.3 mag at $z' = 26.5$ mag) because the broadband images used in this work were smoothed to match the NB711 seeing size before making the photometry.

In order to study the properties of LAEs by SED fitting, the rest-frame optical photometry (i.e., IRAC photometry) is needed. Sixteen out of twenty-four LAEs are in IRAC images (hereafter IRAC sample). Since the angular resolution of IRAC images is not excellent, some LAEs are contaminated by nearby objects. In order to examine whether or not neighboring objects affect the photometry of LAEs, we simultaneously fitted all neighboring objects within a $10''$ radius with GALFIT (Peng et al. 2002) and subtracted them from the original image. In the GALFIT process, we masked the LAEs out so that the accurate sky estimation can be obtained. We then performed aperture photometry of the LAEs from the residual images. We only selected LAEs of which magnitude differences between the original images and the residual images are less than 0.1 mag as isolated LAEs. Finally, we have 12 isolated objects. We divided these 12 LAEs into four groups based on their brightness in the rest-frame UV and optical wavelengths. Group I is for two LAEs that are detected above the 2σ limiting magnitudes in all bands used in the SED fitting process (i.e., I_c, z', IRAC 3.6 μm, and 4.5 μm). One of them, 35915, is spectroscopically confirmed to be at $z = 4.82$. The emission line does not show a doublet profile in $R \sim 2000$ spectrum obtained by GMOS on the Gemini telescope (M. Ouchi et al. 2010, in preparation). With the given resolution, this can rule out the possibility that the object is an [O II] emitter. Moreover, there seems to be a continuum break at the wavelength shortward of the line. Two LAEs are classified as group II, which is an LAE detected in two bands: one in Subaru optical and one in IRAC bands. One LAE is classified as group III which is not detected in the I_c and z' bands but detected in both 3.6 μm and 4.5 μm bands. Group IV is for seven LAEs that are not detected above the 2σ limiting magnitudes in three or more bands. In the SED fitting process, it is necessary that an LAE should be detected above 2σ magnitude limit in more than two bands; therefore, we can use only group I–III LAEs. Hereafter, we call group I–III LAEs the SED fitting sample. The montage images of LAEs are shown in Figures 4, 5, 6, and 7
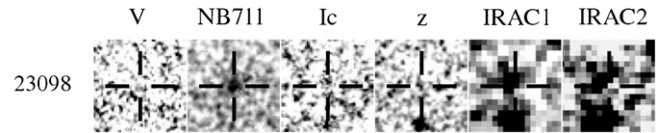

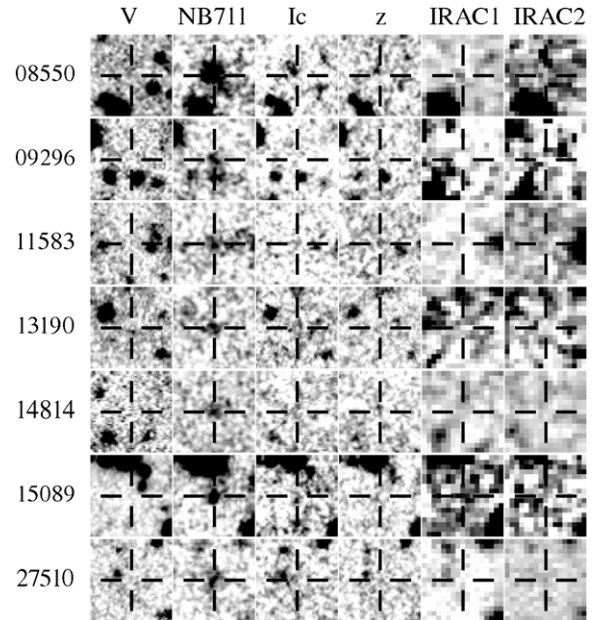**Figure 6.** Same as Figure 4 but for group III LAE.

Figure 7. Same as Figure 4 but for group IV LAEs.

for group I, II, III, and IV, respectively.[9] Aperture photometry of the isolated LAEs is summarized in Table 1. Neighboring objects are seen around some of the group I–II LAEs, but note that the neighboring objects do not affect the photometry more than 0.1 mag. It is noteworthy that the object 23098 in group III is undetected in all optical bands except for the NB711 image, while a bright object is seen close to 23098 with a slight offset in IRAC 3.6 μm and 4.5 μm images. Our aperture photometry includes the light from this object. However, we cannot rule out the possibility that the object is a foreground red object. When we subtract the object, the aperture magnitudes in IRAC bands are fainter than 2σ limiting magnitudes. Thus, it should be kept in mind that the SED of this object may be contaminated.

4. SELECTION BIAS

In this section, we check the sample bias in two point of views: bias on selecting the isolated LAEs and bias on choosing the SED fitting sample. Figure 8(a) shows the distributions of rest-frame Lyα EWs of all LAEs, IRAC sample, isolated LAEs (group I–IV), SED fitting sample (group I–III), and the compared LAE sample (see Section 7). The rest-frame Lyα EWs are calculated by assuming that all LAEs are at $z = 4.86$ and the Lyα emission line falls into the center of the NB711 band (Table 2). Note that the values may be underestimated if the LAEs are not exactly at $z = 4.86$, i.e., the Lyα emission line does not fall into the center of the NB711 band. In addition, the EWs of 20 objects (from the 24 LAEs) are further underestimated due to the 2σ upper limit on I_c magnitudes. For the spectroscopically

---

[9] The object adjacent to 22962, which is very bright in the NB711 band, is a separate object and is likely to be a low-redshift emitter, because it is detected in the V band and does not satisfy the $V - I_c > 1.55$ criterion.

Table 1
Aperture Photometry of Isolated LAEs

ID	Field	V[a,b] (mag)	NB711[a] (mag)	I_c[a,c] (mag)	z'[a,c] (mag)	3.6 μm[a,d] (mag)	4.5 μm[a,d] (mag)
				Group I			
30702	GOODS-N	28.37 ± 0.69	25.46 ± 0.18	26.25 ± 0.36	26.12 ± 0.36	24.97 ± 0.14	25.36 ± 0.22
35915	GOODS-N	>28.51	25.06 ± 0.12	25.79 ± 0.25	25.61 ± 0.24	25.06 ± 0.16	25.60 ± 0.27
				Group II			
12766	GOODS-FF	>28.51	25.81 ± 0.23	>26.50	26.33 ± 0.42	25.12 ± 0.35	>25.05
22962	GOODS-N	>28.51	25.62 ± 0.20	26.26 ± 0.37	>26.38	26.06 ± 0.35	>26.24
				Group III			
23098	GOODS-FF	>28.51	25.85 ± 0.24	>26.50	>26.38	24.42 ± 0.20	24.21 ± 0.23
				Group IV			
08550	GOODS-FF	>28.51	24.39 ± 0.07	26.14 ± 0.33	>26.38	>25.42	>25.05
09296	GOODS-FF	>28.51	25.83 ± 0.24	>26.50	>26.38	>25.42	>25.05
11583	GOODS-FF	>28.51	25.57 ± 0.19	>26.50	>26.38	>25.42	>25.05
13190	GOODS-FF	>28.51	25.78 ± 0.23	>26.50	>26.38	>25.42	>25.05
14814	GOODS-FF	>28.51	25.84 ± 0.24	>26.50	>26.38	>25.42	>25.05
15089	GOODS-FF	>28.51	25.27 ± 0.15	>26.50	26.30 ± 0.42	>25.42	>25.05
27510	GOODS-N	>28.51	25.56 ± 0.19	>26.50	>26.38	>25.42	>25.05

Notes.

[a] Errors are 1σ values.

[b] Upper limits are 1σ values at $2\farcs5$ diameter aperture.

[c] Upper limits are 2σ values at $2\farcs5$ diameter aperture.

[d] Upper limits are 2σ values at $2\farcs4$ diameter aperture.

Table 2
Best-fit Results

ID	Field	Rest Lyα EW[a] (Å)	log[Mass] ($M_\odot$)	log[Age] (yr)	$E(B-V)$ (mag)	log[SFR] ($M_\odot$ yr^{-1})	χ_ν^2	q[b]
				Group I				
30702	GOODS-N	14 (51)	$9.61^{+0.99}_{-0.37}$	$7.49^{+2.50}_{-0.62}$	$0.28^{+0.10}_{-0.28}$	$2.15^{+0.33}_{-1.39}$	0.02	1.32
35915	GOODS-N	40 (202)	$9.39^{+0.72}_{-0.37}$	$7.39^{+1.87}_{-0.62}$	$0.20^{+0.09}_{-0.20}$	$2.03^{+0.32}_{-1.08}$	0.08	1.16
				Group II				
12766	GOODS-FF	$>11(>44)$	$9.29^{+1.59}_{-1.40}$	$6.97^{+3.33}_{-1.35}$	$0.30^{+0.14}_{-0.3}$	$2.32^{+0.37}_{-1.66}$	44.90	<1.44
22962	GOODS-N	10(39)	$8.60^{+1.23}_{-0.71}$	$6.87^{+2.50}_{-0.83}$	$0.14^{+0.10}_{-0.14}$	$1.74^{+0.28}_{-1.15}$	46.63	2.27
				Group III				
23098	GOODS-FF	$>10(>11)$	$10.69^{+1.01}_{-0.60}$	$8.64^{+1.66}_{-1.56}$	$0.40^{+0.58}_{-0.32}$	$2.14^{+1.40}_{-1.06}$	47.05	<1.01

Notes.

[a] The rest-frame Lyα EWs are determined by assuming that all LAEs are at $z = 4.86$ except for 35915. Values in parentheses indicate the EW in case of using broadband images both redward and blueward of Lyα wavelength to estimate the continuum.

[b] The clumpiness parameter (see the text for further details).

confirmed LAE (35915), the Lyα emission line is in the NB711 band, but is out of NB711 FWHM range. By considering the transmission curve of the NB711 filter, the corrected EW is estimated to be 40 Å (Table 2) and is used hereafter. As a cross-check, we also examine the EW from the spectrum and find that it is consistent with that obtained from the imaging. The EWs of LAEs are distributed from 10 Å (the selection limit) to 55 Å. Figures 8(b) and (c) show the distributions of z' magnitudes and $I_c - z'$ colors, respectively. The leftmost bins in Figures 8(b) and (c) represent LAEs with z' magnitudes fainter than 26.5 mag and with magnitudes fainter than 2σ limiting magnitudes in both I_c and z' bands, respectively. The large number of LAEs in the leftmost bins of both figures imply that most of the LAEs have faint UV continuum. As seen in Figures 8(a)–(c), the isolated LAEs (red open histogram)

occupy the same range of distributions as the whole sample at $z = 4.86$ (orange histogram). In order to check whether or not selecting isolated sources in IRAC images can cause any bias in the properties of the whole sample of LAEs, we applied the Kolmogorov–Smirnov test (K-S test) to the distributions of the properties of all the LAEs at $z = 4.86$ and the isolated LAEs. We could not reject the null hypothesis that the rest-frame Lyα EW, z' magnitude, and $I_c - z'$ color distributions of these two samples are drawn from the same populations at more than 95% confidence levels. However, we could not use all the isolated samples in SED fitting because of their faintness either in rest-frame UV or optical wavelengths. To investigate if the SED fitting in the following section can represent all populations of LAEs at this redshift, we have to compare the SED fitting sample (group I–III, green histogram) to all LAEs (orange histogram). It
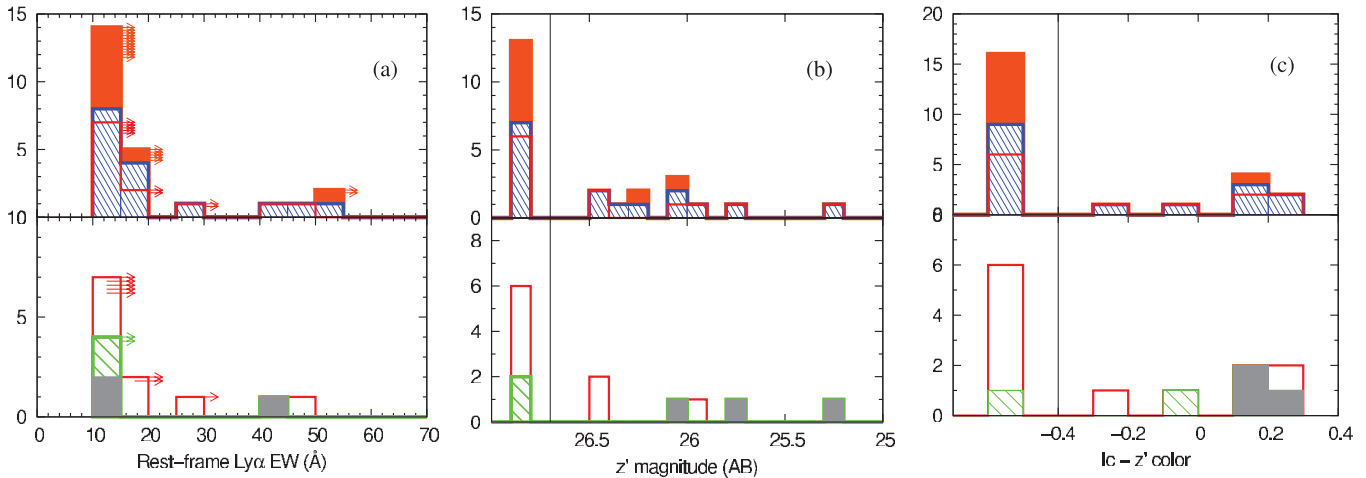
Figure 8. Distributions of rest-frame Lyα EW, z'-band magnitude, and $I_c - z'$ color of LAE samples. We divide each figure into two panels for display purposes. In the top panel, an orange histogram shows the distribution of all 24 LAEs at $z = 4.86$, while the blue and red histograms are for the IRAC samples and the isolated LAEs (group I–IV), respectively. In the bottom panel, red histograms refer to the isolated LAEs (the same as in the top panel). Group I–III LAEs are shown in green histograms. Distributions of group I LAEs and 12766 from group II LAEs (the compared LAE sample; see Section 7) are shown in gray histograms. Arrows shown in panel (a) represent the lower limits in Lyα EWs of LAEs; the number of arrows directly corresponds to the number of LAEs with Lyα EW lower limits. Note that the leftmost bins in panels (b) and (c) indicate, respectively, the LAEs fainter than $z' = 26.5$ mag and LAEs that are not detected above 2σ limiting magnitudes in neither the I_c nor z' bands.

(A color version of this figure is available in the online journal.)

is seen in Figure 8(a) that group I–III LAEs represent both high- and low-EW LAEs. However, we can see from Figures 8(b) and (c) that the SED fitting sample is biased toward the bright UV luminosity and red $I_c - z'$ colors as we neglect the leftmost bins where magnitudes are unreliable. In addition, Table 1 shows that the SED fitting sample is relatively bright in IRAC bands as compared to all isolated LAEs, implying brighter luminosity in the rest-frame optical wavelength. Thus, we conclude that the SED fitting and the results hereafter are for the LAEs which have the brighter rest-frame UV and optical magnitudes, and the relatively redder UV colors.

5. STELLAR POPULATION SYNTHESIS MODEL AND SED FITTING

In this paper, we intend to compare the stellar populations of the LAEs to those of LBGs at the same redshift by Yabe et al. (2009). In order to make a fair comparison, we used the same stellar population synthesis model as that used in Yabe et al. (2009). The model SEDs were obtained with the Bruzual & Charlot (2003, hereafter BC03) synthesis code. We used the Padova 1994 evolutionary track as recommended by BC03. A Salpeter (1955) initial mass function (IMF) with lower and upper mass cutoffs of 0.1 and $100\,M_\odot$ is assumed. We made models by fixing the metallicity at $0.2\,Z_\odot$[10] and assuming a constant star formation history. BC03 use quasi-logarithmic 221 time steps from 0.1 Myr to 20 Gyr. Time steps were adopted to 51 logarithmic steps both to reduce the calculation time and to avoid dealing with an unequally spaced scale of the original 221 models. The age of the universe at $z \sim 5$ is ~ 1.2 Gyr. However, as a cross-check on the fits, we allowed the age up to the oldest one available in BC03. The effect of dust attenuation is taken into account by using the Calzetti

extinction law (Calzetti et al. 2000), changing the color excess $E(B - V)$ from 0.0 mag to 0.8 mag with a step of 0.01. The attenuation by the IGM is calculated using the prescription by Madau (1995). The model spectra were then convolved with the appropriate filter transmission curves to give model fluxes. This is exactly the same as done in Sawicki & Yee (1998). Except for one spectroscopically confirmed LAE (35915; $z = 4.82$), the redshift was fixed at $z = 4.86$ under the assumption that the Lyα emission of our LAE sample is detected at the center of the NB711 bandpass.

Some of the observed SEDs, including one spectroscopically confirmed LAE, show a significant excess in the 3.6 μm band as compared with the magnitude in the 4.5 μm band. This is likely to be due to the Hα emission line, which falls into IRAC ch1 (3.6 μm) at this redshift. The excess is also seen in some fraction of $z \sim 5$ LBGs (Yabe et al. 2009). The SED model including Hα emission shows a better fit (Chary et al. 2005; Finkelstein et al. 2008; Yabe et al. 2009). As adopted by Yabe et al. (2009), the spectrum of Hα emission is included in the synthesis model spectrum by the following process. The luminosity of the Hα emission is calculated from the SFR of the model by using the relation by Kennicutt (1998).[11] The dust extinction to the line (Calzetti et al. 2000) is assumed to be the same as the dust extinction to the stellar component.[11] The Hα flux density is finally put into each model SED. The existence of Hα emission line in the models makes the fit better without adding a free parameter (Yabe et al. 2009).

We use the SEDfit software (M. Sawicki 2010, in preparation), which is an evolved version of the SED-fitting software used in Sawicki & Yee (1998) and subsequent papers, including the $z \sim 5$ LBG study by Yabe et al. (2009). After we produce a suite of model fluxes by the means described above, the best-fitting model is found by means of a maximum likelihood test for each object. For objects detected in all bands (i.e., our group I objects), this test is the standard χ^2 minimization. For objects

---

[10] Fixing the metallicity at the lower abundance $(0.005\,Z_\odot)$ does not significantly change the fitting results. The stellar masses derived from the lower metallicity model differ from those derived from the $0.2\,Z_\odot$ model by $\sim 10\%$ at most. The average differences of age, color excess, and SFR are $\sim 50\%$, ± 0.2 mag, and $\sim 5\%$, respectively.

[11] Adopting this relation may be disputable. Dependences on metallicities and differences of extinction to stellar continuum and nebular emission are discussed by Yabe et al. (2009, their Appendix B).
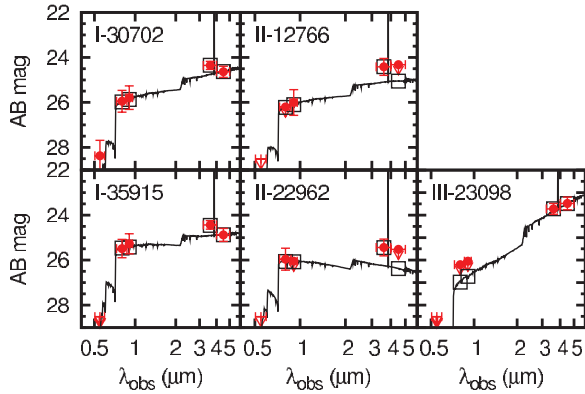
Figure 9. Observed SEDs and the best-fitting models for group I–III LAEs. In each panel, the observed SED is shown with filled circles; the best-fitting model SED is indicated by open squares. The solid line represents the best-fitting model spectrum with Hα emission line. Arrows indicate the 2σ upper limits. V-band photometry is also shown in the figures but is not used in SED fitting.

(A color version of this figure is available in the online journal.)

that are undetected in some of the bands (i.e., group II and III objects), SEDfit employs a modification of the χ^2 formalism: as is standard in the χ^2 approach, for the filters in which the object is detected the maximum likelihood calculation considers the likelihood that the detected data deviate from the model given the uncertainties; for the undetected filters, the calculation adds in the likelihood that a given model would/would not have been detected given the upper limit of the non-detection. For more details on this technique, see M. Sawicki (2010, in preparation).

In this paper, we constructed an observed SED of each individual object from the photometry in the I_c, z', IRAC 3.6 μm, and 4.5 μm bands. As explained in Section 2, we do not use V-band photometry in the SED fitting process in order to avoid the uncertainty due to IGM absorption. IRAC 5.8 μm and 8.0 μm photometry is not used because of the low S/N of the images. Including the upper limits of the photometry in IRAC 5.8 μm and 8.0 μm bands does not usefully improve the fitting. Free parameters in our fitting process are age, color excess, and scaling normalization. The SFR is obtained from the scaling normalization. We then find the stellar mass by using the age and SFR (Sawicki & Yee 1998).

6. RESULTS

The fitting results are summarized in Table 2. Errors in the table are at 68% confidence level and are determined as follows. The Monte Carlo realizations for each object are performed; we vary the input fluxes within their photometric uncertainties, rederive the best-fitting model, and repeat it 100 times. The error on an individual parameter is then in the 68% range of the realizations in that parameter. The best-fitting model spectra are shown with the observed SEDs in Figure 9.

The derived stellar masses range from 10^8 to 10^{11} $M_\odot$ with the median value of 2.5×10^9 $M_\odot$. A typical error on the stellar mass is ∼0.9 dex. By considering only group I LAEs, which are detected in all bands used in the SED fitting, the stellar mass is on the order of 10^9 $M_\odot$ with the smaller typical error of ∼0.6 dex. A relationship between the stellar masses and the rest-frame optical absolute magnitudes is shown in Figure 10(a); the optical absolute magnitudes were calculated from the [4.5 μm] magnitudes by assuming $f_\lambda \propto \lambda^\beta$ with β derived from the $z' - $ [4.5 μm] color of an individual object. For LAEs with an upper limit, we used the upper limit to estimate
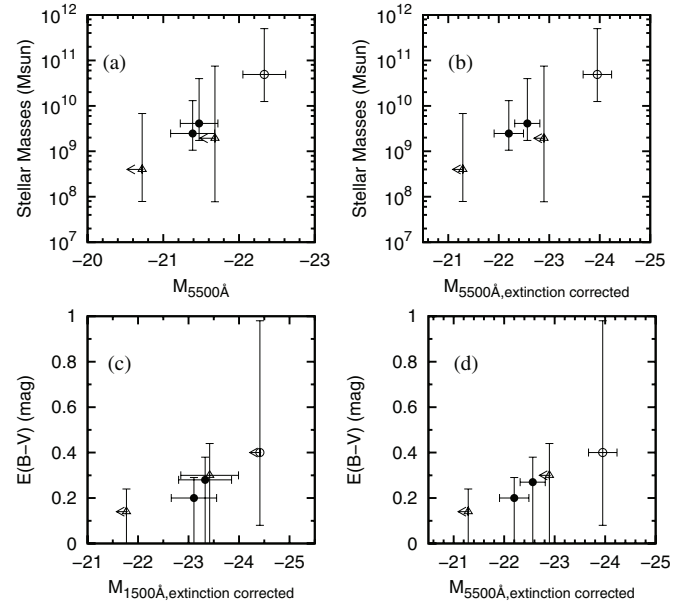

Figure 10. Plots of derived stellar masses and color excesses of group I–III LAEs at $z = 4.86$ against the rest-frame UV or optical absolute magnitudes. Filled circles, open triangles, and open circles represent group I, II, and III LAEs, respectively. Vertical error bars represent the 68% errors as described in the text. Arrows indicate the objects whose absolute magnitudes were calculated from the upper limits.

the magnitude. Despite the small size of the sample, the rest-frame optical luminosity is likely to be a tracer of the stellar mass. The relationship between the stellar mass and extinction-corrected optical absolute magnitude also shows a correlation (Figure 10(b)). A mass-to-light ratio is not perfectly linear; it becomes larger in the brighter LAEs. This trend is similar to the results of LBGs at the same redshift by Yabe et al. (2009) which will be discussed in more detail in the following section. From the relationship between the stellar mass and the rest-frame optical luminosity, it is implied that most LAEs at $z = 4.86$, which could not be detected above 2σ limiting magnitudes in the 4.5 μm band (Table 1), are likely to have stellar masses lower than 10^9 $M_\odot$.

The best-fitting stellar ages are in a wide range from 7.4 Myr to 437 Myr with the median age of 25 Myr. Although we did not limit the model age to the age of the universe at $z = 4.86$ (∼1.2 Gyr), there is no LAE with the best-fitting age exceeding the cosmic age. The typical error in the age of each object is very large (∼1.7 dex). The uncertainties of the ages cover most of the age range available in the models. Thus, it is difficult to draw any conclusion on their correlation.

The color excesses $E(B - V)$ range from 0.14 mag to as high as 0.40 mag. The median value is 0.27 mag. The typical error in $E(B - V)$ is ∼0.2 mag. It is seen in Figures 10(c) and (d) that dust extinction seems to show some correlation with both rest-frame UV and optical magnitudes. However, the trends are less significant if we consider the uncertainties and upper limits. Similarly, no trend between the color excess and other fitting properties can be seen when we take the uncertainties into account (Figure 11). As mentioned in the last part of Section 3, IRAC photometry of the group III LAE (23098) may be contaminated. By removing the LAE from group III, the derived color excesses are 0.14–0.30 mag; any correlations between the dust extinction and magnitudes or other properties cannot be seen. The presence of some amount of color excess
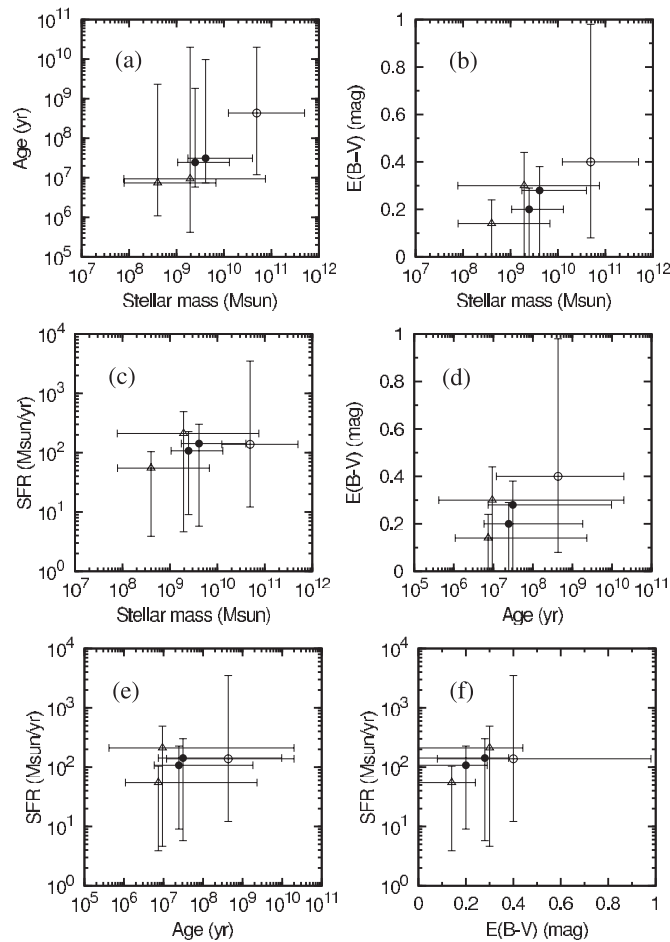
Figure 11. Relations of output parameters from SED fittings for group I–III LAEs at $z = 4.86$. Filled circles, open triangles, and open circles represent group I, II, and III LAEs, respectively.

indicates that LAEs at this redshift are not free from dust, which is consistent with what Finkelstein et al. (2007, 2008, 2009) found for LAEs at $z \sim 4.5$. Many authors (Neufeld 1991; Hansen & Oh 2006; Finkelstein et al. 2009) proposed that the presence of dust in clumpy clouds can enhance the Lyα EW of a galaxy. To test this hypothesis, we estimated the clumpiness parameter (q): $q\tau$ is the Lyα line opacity, where τ is an optical depth for the continuum (Finkelstein et al. 2008). If $q < 1$, the Lyα EW is enhanced on the hypothesis that Lyα photons suffer less extinction than the continuum photons and the clumpy cloud model would be supported. We calculate q from the ratio of observed and intrinsic Lyα luminosities. The observed Lyα luminosity is derived from the observed Lyα EW and the continuum flux density, while the intrinsic one is calculated from the Hα luminosity by assuming case B recombination. Except for 12766 and 23098, which show upper limits on the q parameter, all LAEs show $q > 1$ (Table 2) suggesting that Lyα photons suffer from dust extinction larger than the continuum. The uncertainty of the q value is large; nevertheless, the q values are all near 1–2 suggesting that although the Lyα emission appears to be more attenuated than the continuum, the difference is not so large. In Section 3, however, we mentioned that the observed Lyα EWs may be underestimated if the Lyα emission line does not fall into the central part of the NB711 filter and are further underestimated due to the non-detection in the I_c band for some LAEs. Underestimation of the Lyα EW results in the overestimation of the q parameter. Accordingly,

the objects without spectroscopic confirmation, i.e., 30702 and 22962, could have q values less than those shown in Table 2, if their Lyα line did not fall into the central part of the NB711 filter. The spectroscopic observations are desirable in investigating the real Lyα EWs and q values of the LAEs.

The best-fitting SFRs of LAEs range from 55 $M_\odot$ yr^{-1} to 209 $M_\odot$ yr^{-1}. The median value of the derived SFRs is 132 $M_\odot$ yr^{-1}. The typical error on the SFR for each object is $\sim$0.9 dex. These SFRs are much higher than the SFRs of LAEs from other studies (e.g., Gawiser et al. 2007; Nilsson et al. 2007). This is probably due to the selection effect. Our SED fitting sample has to be bright enough to be detected in either ground-based broadbands or IRAC bands or both. Thus, the selected LAEs are more luminous, which results in the higher SFRs. The relations between the SFR and other fitting properties are shown in Figures 11(c), (e), and (f). Looking only at the best-fitting values, we see that the SFR seems to show correlation with stellar mass and dust extinction. However, the correlations are not significant when we consider the uncertainties or exclude the group III LAE.

Since some of the LAEs show very young ages, the effect of nebular continuum emission may not be negligible. We examine the effects of nebular emission on the SED fitting results and describe more details in the Appendix. Briefly, we found that the stellar mass estimation of all LAEs is robust ($\pm$0.04 dex). Age, color excess, and SFR for group I LAEs are also robust ($\pm$0.24 dex, $\pm$0.02 mag, and $\pm$0.10 dex, respectively). For group II and III LAEs, age, color, and SFR do not agree well with each other, but agree within their large uncertainties. Hα emission accounts for the largest expected nebular line emission detected from our LAEs. Including Hα emission in the model spectrum when we performed SED fitting in the last section is likely to be the reason why adding the other nebular emissions give similar results.

7. COMPARISONS TO LBGs AT $z \sim 5$

In this paper, we aim at comparing the derived stellar populations of LAEs at $z \sim 5$ to those of LBGs at the same redshift and in the same field by Yabe et al. (2009). Yabe et al. (2009) used LBGs at $z \sim 5$ with $z' < 26.5$ mag selected by Iwata et al. (2007); they used the same data set and the same V-dropout criteria as those used in this study. In addition, the SED models and the fitting technique are also the same. In order to make a fair comparison, we used only LAEs whose z'_{total} magnitudes are brighter than 26.5 mag. Because part of the LBGs are spectroscopically confirmed with the mean redshift of $z \sim 4.7$ (Ando et al. 2007; Kajino et al. 2009), taking the same limit on the z' magnitude is equivalent to taking the same limit on rest-frame UV luminosity. There are six LAEs with $z'_{total} < 26.5$ mag in the IRAC isolated sample. Two of them are in the group I LAEs; one is in group II (12766). The others are group IV LAEs for which we could not perform SED fitting. Therefore, we used three LAEs from groups I and II for comparison. Among these three LAEs, one (35915) appears in the Iwata et al. (2007) catalog and also in Yabe et al. (2009). Though we used the same set of broadband data as Iwata et al. (2007) to select the sample, the images in our case were smoothed to have the same seeing size as that of the NB711 image before performing photometry (Section 2.1.2). Accordingly, magnitudes measured from the images before and after smoothing are not necessarily the same.

From 617 LBGs at $z \sim 5$ (Iwata et al. 2007), Yabe et al. (2009) selected 170 LBGs by eye inspection as isolated objects both in the z' band and in IRAC images. The 170 LBGs are
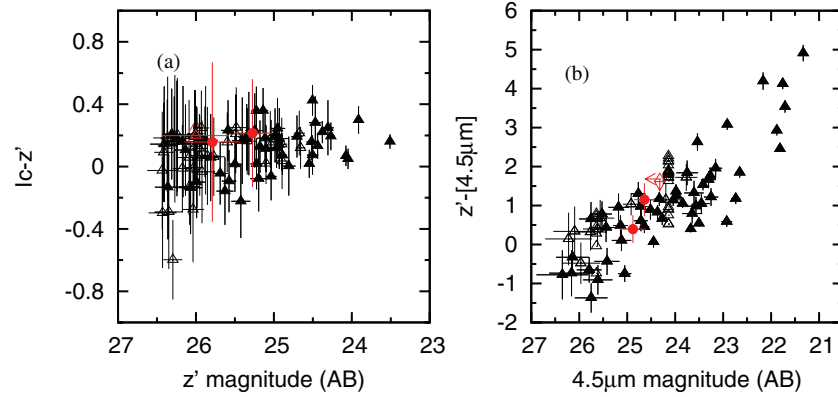
Figure 12. (a) $I_c - z'$ vs. z' magnitude diagram; (b) $z' - [4.5\,\mu m]$ vs. $4.5\,\mu m$ magnitude diagram. Group I LAEs and 12766 from group II are indicated by the red filled circles and the red open triangle, respectively. LBGs in category 1 are plotted in filled triangles; those in categories 2 and 3 are plotted with black open triangles. Arrows show the limits in magnitudes or colors. Errors of LBGs are taken from Yabe et al. (2009).

(A color version of this figure is available in the online journal.)

divided into four categories according to their detection in the $3.6\,\mu m$ and $4.5\,\mu m$ filters. The LBGs that are detected in both the $3.6\,\mu m$ and $4.5\,\mu m$ images are in category 1, while those only detected in either $3.6\,\mu m$ or $4.5\,\mu m$ are put in category 2 or 3, respectively. The rest that are detected in neither the $3.6\,\mu m$ nor $4.5\,\mu m$ images are in category 4. We used category 1, 2, and 3 LBGs in the comparison. Yabe et al. (2009) performed the SED fitting for 64 LBGs in category 1. For category 2 and 3 LBGs, we refitted them by using an upper limit either in the $4.5\,\mu m$ or the $3.6\,\mu m$ band, respectively. Seventeen LBGs are best fitted with stellar ages larger than the cosmic age at $z \sim 5$ (~ 1.2 Gyr). The reason for the large ages is considered to be the assumption of constant star formation history or low-z interlopers (Yabe et al. 2009; Sawicki & Yee 1998; Papovich et al. 2001). The derived ages are generally older than those derived by assuming other star formation histories. We thus excluded these objects in the following comparison. We eventually have 88 LBGs from categories 1, 2, and 3 to compare with our three LAEs from groups I and II. It should be noted that since the NB711 filter covers only a small fraction of the redshift range, LAEs that are not in this redshift range are expected among the LBG sample.

Before proceeding to the comparison between stellar populations of LAEs and those of LBGs, we try to figure out what their photometry can tell us without SED fitting. Another thing which should be kept in mind is that three LAEs that are used for comparison with the LBGs in this section (i.e., group I LAEs and 12766, hereafter "compared LAE sample") are not necessarily good representatives for all LAEs at $z = 4.86$. As shown in Figure 8, the compared LAE sample (gray histogram) is relatively bright and has a comparatively red UV color as compared to the whole LAE sample. Figure 12 shows the color–magnitude diagrams of the compared LAE sample and the LBGs at $z \sim 5$. No clear trend is seen between the z' magnitude and the $I_c - z'$ color (Figure 12(a)). The figure shows that the LAEs occupy the faint part of the z'-magnitude distribution and the red part of the $I_c - z'$ color distribution of the LBGs. Distribution of these LAEs at the faint part of UV luminosity among LBGs may support the deficiency of strong Lyα emission among bright LBGs claimed by Ando et al. (2006), though the sample size is only three. Figure 12(b) shows the color–magnitude diagram of the $z' - [4.5\,\mu m]$ color and $4.5\,\mu m$ magnitude. The $z' - [4.5\,\mu m]$ colors of LBGs spread over a wide range from -1 to 5 mag. The LAEs are on the distributions of LBGs, but they are located in the slightly fainter part in the $4.5\,\mu m$ band magnitude and the relatively bluer part of the color distributions than the LBGs.

Output parameters of SED fitting are plotted against the rest-frame UV and optical luminosities in Figure 13. The top panels show the comparisons between the derived stellar masses of LAEs and those of LBGs. The stellar masses of the compared LAE sample range from $10^9\,M_\odot$ to $10^{10}\,M_\odot$. In contrast, LBGs are distributed in a larger range from $10^8\,M_\odot$ to $10^{11}\,M_\odot$. It is seen in the figure that the LAEs are located in the region where LBGs are distributed and almost in the middle part of LBGs' distribution. At the same bin of rest-frame UV or optical luminosity, LAEs seem to have comparable masses to LBGs.

Showing no relation between ages and luminosities, Figures 13(c) and (d) indicate that the LAEs again lie on the same part of the LBG's distribution. The median ages are similar; they are 25 Myr and 22 Myr for LAEs and LBGs, respectively. However, age uncertainties of the LAEs cover the whole range of age distribution of the LBGs. It is difficult to draw any conclusion.

Figures 13(e) and (f) show the plots of the derived color excesses against UV and optical absolute magnitudes, respectively. Although the dust extinction of the LAEs is not zero, they seem to lie at a relatively lower region of the color excess distribution of LBGs. At the fixed rest-frame UV or optical luminosity, there seems to be no difference in $E(B - V)$, even if we take the uncertainties into account. Figure 13(e) shows that there is no relation between the dust extinction and the rest-frame UV luminosity. In contrast, Figure 13(f) seems to show a correlation of LBGs between the color excesses and the optical magnitudes. Though we cannot state any correlation for only three LAEs, the LAEs still lie on the correlation of LBGs.

The SFRs are plotted against rest-frame UV and optical absolute magnitudes in Figures 13(g) and (h), respectively. Both figures show a correlation of SFRs of the LBGs with UV (but weak) and optical luminosity. It is seen from the figures that the LAEs are located in the lower part of the LBGs' distribution. A median SFR of the LAEs is $132\,M_\odot\,\mathrm{yr}^{-1}$, while it is $187\,M_\odot\,\mathrm{yr}^{-1}$ for LBGs. Note that the LAEs used in the comparison are biased toward the brightest sample among the whole LAE sample (Section 4), which probably results in the higher SFRs of the LAEs. In conclusion, no significant differences in the stellar properties between LAEs and LBGs are seen at the same luminosity.

A physical reason that makes an LAE an emitter is still unclear. In order to investigate whether or not the difference between LBGs and LAEs has any dependence on the
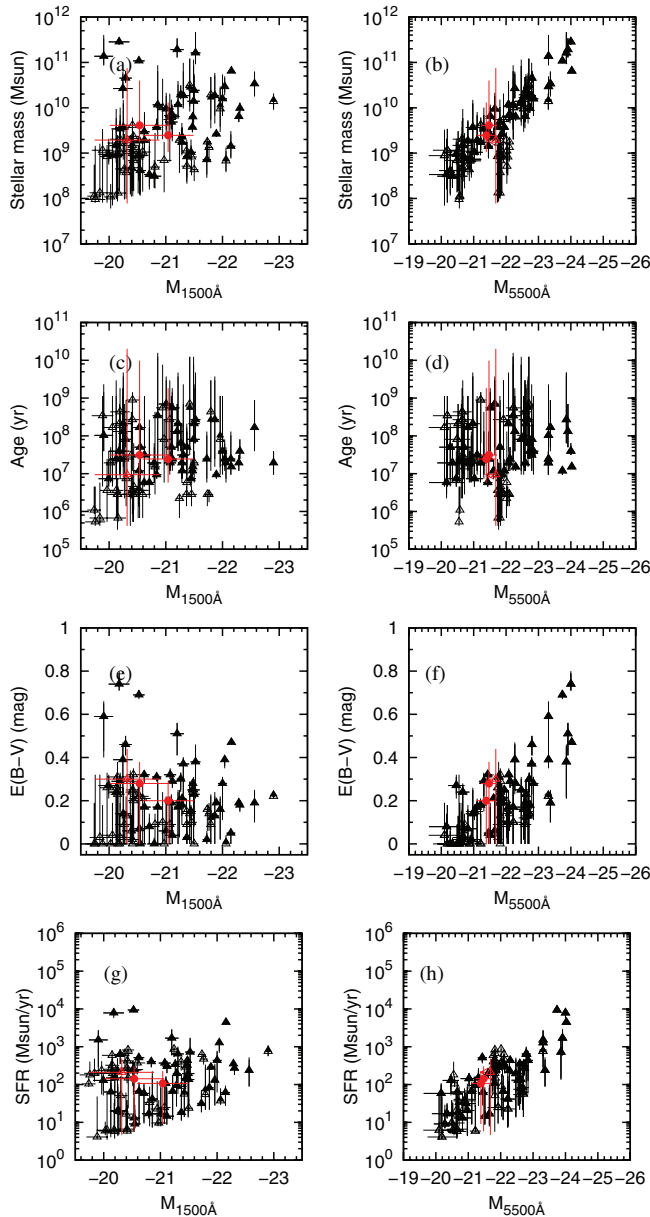
Figure 13. Output parameters of SED fitting against the UV and optical absolute magnitudes. Symbols are the same as those in Figure 12.

(A color version of this figure is available in the online journal.)

Figure 14. Output parameters from SED fitting for group I–III LAEs vs. rest-frame Lyα EWs. Filled circles, open triangles, and open circles represent group I, II, and III LAEs, respectively. LBGs that have spectroscopic Lyα EWs are also shown in filled squares.

8. SUMMARY

In this paper, we studied the stellar properties of LAEs at $z = 4.86$ using SED fitting. Using narrowband and broadband observations by the Suprime-Cam on the Subaru Telescope, 24 LAEs were selected in the area of ~508.5 arcmin^2 around the GOODS-N field. In addition to the optical photometry, we obtained the mid-infrared photometry from data taken by IRAC on the *Spitzer Space Telescope* in the GOODS-N field as well as the surrounding area in order to cover most of the Subaru area. We selected 12 LAEs that are isolated from neighboring objects. We performed SED fitting of five LAEs that are detected above 2σ magnitude limits in more than two bands. Selecting those five LAEs could introduce a bias toward bright red galaxies. Model SEDs are built by assuming a constant star formation history with a fixed metallicity of $0.2\,Z_\odot$, the Salpeter IMF ranging from $0.1\,M_\odot$ to $100\,M_\odot$, and the extinction law of Calzetti et al. (2000). The derived stellar masses of the LAEs range from 10^8 to $10^{10}\,M_\odot$ with the median value of $2.5 \times 10^9\,M_\odot$. The derived ages cover wide range from 7.4 Myr to 437 Myr with the median value of 25 Myr. The color excess is between 0.1 and 0.4 mag, indicative of the presence of some amount of dust. SFRs are in the range of 55–209 $M_\odot$ yr^{-1}. The median color excess and SFRs are 0.27 mag and 132 $M_\odot$ yr^{-1}, respectively. The high SFRs are probably due to the selection effect; we selected the LAEs that are bright enough to be detected in rest-frame UV and optical bands, which results in selecting the LAEs with the higher SFRs. We investigated the correlations between the stellar properties derived by SED fitting and the photometric properties of LAEs and found no significant correlation due to both the small size of the sample and the large uncertainty in the fitting results.

The main objective of this study is to compare LAEs to LBGs at the same redshift. LBGs were selected by *V*-dropout criteria (Iwata et al. 2007). Their stellar populations were derived by Yabe et al. (2009). Because those LBGs are selected from the same set of data, and stellar population was derived by the same

EWs of Lyα emission, we plotted the output parameters of SED fitting against the rest-frame Lyα EWs in Figure 14. Group I–III LAEs are plotted with five LBGs that have spectroscopic Lyα EWs (Ando et al. 2004; Kajino et al. 2009). Arrows in the figures represent the lower limits on EWs of the LAEs; their I_c magnitudes are fainter than the 2σ limiting magnitude. Note that, except for one spectroscopically confirmed LAE, the Lyα EWs of LAEs are likely to be lower limits if their Lyα emission lines do not fall into the center of the NB711 band. According to the figure, we cannot find any significant correlation between the stellar properties and the rest-frame Lyα EWs. Recently, Kornei et al. (2010) studied these relations for $z \sim 3$ LBGs with spectra. They found that the stellar mass does not correlate with the Lyα EW, while large Lyα EW is seen in older, lower SFR, and less dusty LBGs. Such trends are difficult to isolate with only three LAEs. A larger sample at $z \sim 5$ is required to see clearer relations, if any, and to be definitive.
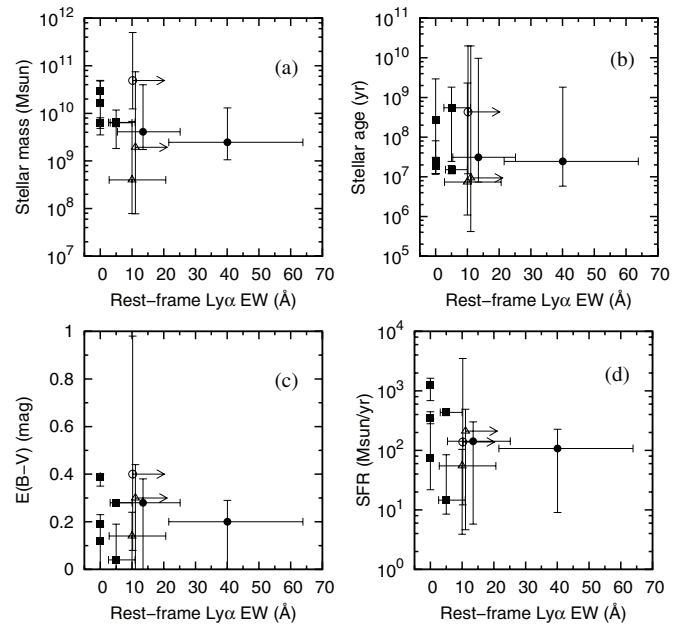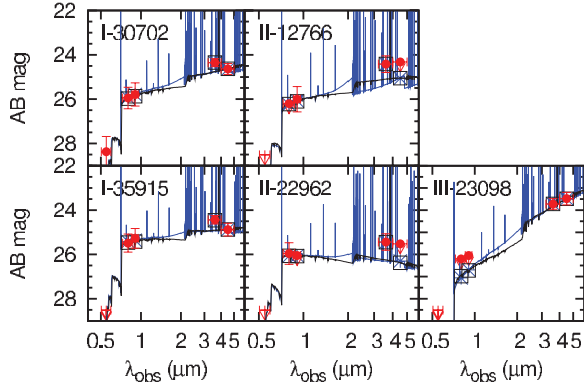
Figure 15. Observed SEDs and the best-fitting models for LAEs in group I (left panel), group II (middle panel), and group III (right panel). In each panel, the observed SED is shown with filled circles; the best-fitting model SEDs are indicated by open squares and asterisks for the BC03 and PEGASE models, respectively. The black line represents the best-fitting BC03 model spectrum with Hα emission line, while the blue one represents the PEGASE model. 2σ upper limit of *V*-band photometry is also shown with the arrow; however, the data are not used in SED fitting.

(A color version of this figure is available in the online journal.)

SED fitting model, we can make a fair comparison between their stellar populations. We compared 3 LAEs to 88 LBGs down to the same UV luminosity limit. These three LAEs are the brightest and reddest ones among the whole LAE sample in this study. The comparisons of SED-fitting parameters show that LAEs are located in the region where LBGs are distributed; the physical properties of LAEs and LBGs occupy similar parameter spaces. At the same rest-frame UV or optical luminosity, there is no difference in stellar properties between LAEs and LBGs. In order to figure out properties that control the Lyα EWs, we plotted the output parameters against the rest-frame Lyα

EWs ranging from 0 to 40 Å. We could not find any significant correlation between them. A larger sample is needed to see if any correlation of Lyα EW exists.

APPENDIX

EFFECTS OF NEBULAR EMISSION

In order to investigate the effects of nebular emission on the synthesis models, we used the stellar population synthesis model by Fioc & Rocca-Volmerange (1997, Fioc & Rocca-Volmerange 1999, hereafter PEGASE). The PEGASE can add nebular emission (continuum and emission lines) to the model spectrum. The hydrogen emission lines are computed from the number of Lyman continuum photons by assuming case B recombination. Other emission lines are calculated from the observed ratios to Hβ for typical local starbursts (Fioc & Rocca-Volmerange 1997). Other prescriptions are the same as those used in the case of the BC03 model described in the main text. We used the Salpeter (1955) IMF with lower and upper mass cutoffs of 0.1 and 100 $M_\odot$, respectively, adopted a metallicity of $0.2 Z_\odot$, and assumed a constant star formation history. We re-scaled the age step of PEGASE into the logarithmic scale as we did for the BC03 model. The effect of dust attenuation is taken into account by using the Calzetti extinction law (Calzetti et al. 2000). $E(B-V)$ varies from 0.0 mag to 0.8 mag with a step of 0.01. The attenuation due to the IGM is calculated following
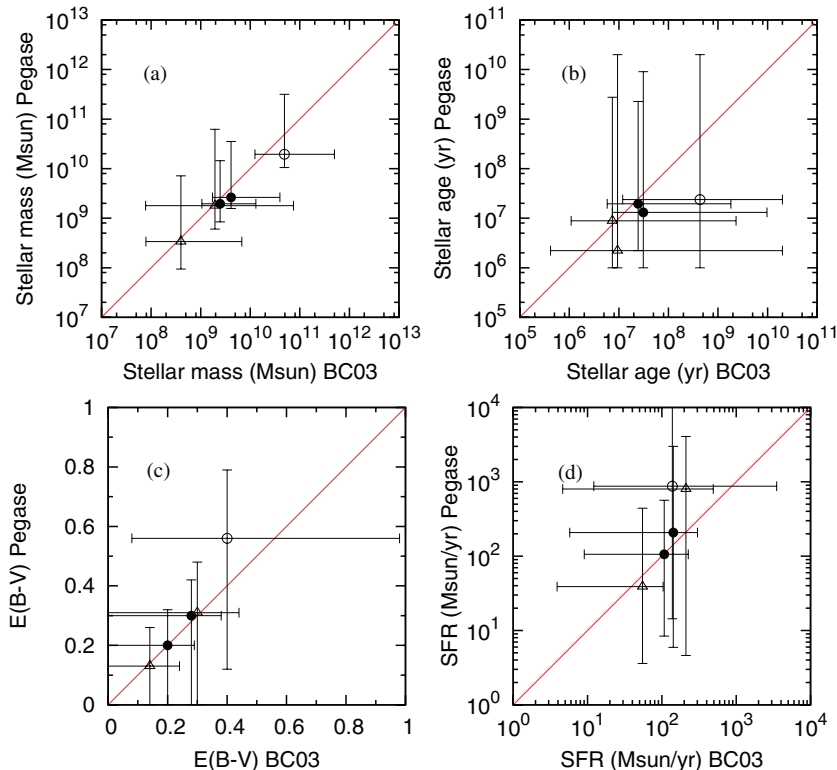

Figure 16. Comparison of output parameters from the BC03 and PEGASE models. Filled circles, open triangles, and open circles represent group I, II, and III LAEs, respectively.

(A color version of this figure is available in the online journal.)

Table 3
Best-fit Results for the PEGASE Model

ID	Field	log[Mass] ($M_\odot$)	log[Age] (yr)	$E(B-V)$ (mag)	log[SFR] ($M_\odot$ yr^{-1})	χ^2_ν
			Group I			
30702	GOODS-N	$9.42^{+1.13}_{-0.22}$	$7.12^{+2.84}_{-1.12}$	$0.30^{+0.12}_{-0.30}$	$2.32^{+1.16}_{-1.54}$	0.001
35915	GOODS-N	$9.29^{+0.87}_{-0.37}$	$7.29^{+2.06}_{-0.95}$	$0.20^{+0.12}_{-0.20}$	$2.03^{+0.73}_{-1.10}$	0.05
			Group II			
12766	GOODS-FF	$9.25^{+1.54}_{-0.47}$	$6.34^{+3.96}_{-0.34}$	$0.31^{+0.17}_{-0.31}$	$2.90^{+0.71}_{-2.24}$	44.88
22962	GOODS-N	$8.53^{+1.33}_{-0.56}$	$6.95^{+2.49}_{-0.95}$	$0.13^{+0.13}_{-0.13}$	$1.59^{+1.05}_{-1.03}$	46.64
			Group III			
23098	GOODS-FF	$10.29^{+1.21}_{-0.27}$	$7.38^{+2.92}_{-1.38}$	$0.56^{+0.23}_{-0.44}$	$2.94^{+1.53}_{-1.78}$	47.05

Madau (1995). The redshift is fixed at $z = 4.86$, except for 35915, which has a spectroscopic redshift (Section 5).

The results obtained for group I–III LAEs with PEGASE are summarized in Table 3. The best-fit spectra are shown as a comparison with the BC03 best-fitting spectra in Figure 15. The comparisons of the resulting parameters are presented in Figure 16. Figure 16(a) shows that the stellar masses derived by both models agree well with each other. The stellar masses obtained by the PEGASE model are on average smaller than those obtained by the BC03 model by about 0.04 dex. As seen in Figure 16(b), the stellar ages of most LAEs derived by PEGASE are younger than those derived from the BC03 models. Inclusion of nebular emission decreases the ages of all LAEs by 0.46 dex on average. However, due to the large uncertainties in determining the stellar ages, the derived ages seem to be in agreement within the uncertainty range. Figure 16(c) shows that the color excesses derived by PEGASE are comparable to those derived using the BC03 model. The average difference is 0.04 mag except for the group III LAE. As seen in Figure 16(d), the SFRs derived by both models seem to be comparable for most of the LAEs. However, rather large differences are seen for the group III LAE and for one in group II (12766). SFRs increase about 0.28 dex on average when nebular emission is included.

REFERENCES

Ajiki, M., Mobasher, B., Taniguchi, Y., Shioya, Y., Nagao, T., Murayama, T., & Sasaki, S. S. 2006, ApJ, 638, 596
Ajiki, M., et al. 2003, AJ, 126, 2091
Ajiki, M., et al. 2004, PASJ, 56, 597
Ando, M., Ohta, K., Iwata, I., Akiyama, M., Aoki, K., & Tamura, N. 2006, ApJ, 645, L9
Ando, M., Ohta, K., Iwata, I., Akiyama, M., Aoki, K., & Tamura, N. 2007, PASJ, 59, 717
Ando, M., Ohta, K., Iwata, I., Watanabe, C., Tamura, N., Akiyama, M., & Aoki, K. 2004, ApJ, 610, 635
Bertin, E., & Arnouts, S. 1996, A&AS, 117, 393
Bouwens, R. J., Illingworth, G. D., Franx, M., & Ford, H. 2008, ApJ, 686, 230
Bouwens, R. J., et al. 2004, ApJ, 616, L79
Bruzual, G., & Charlot, S. 2003, MNRAS, 344, 1000
Calzetti, D., Armus, L., Bohlin, C., Kinney, A. L., Koornneef, J., & Storchi-Bergmann, T. 2000, ApJ, 533, 682
Capak, P., et al. 2004, AJ, 127, 180
Chary, R., Stern, D., & Eisenhardt, P. 2005, ApJ, 635, L5
Cowie, L. L., & Hu, E. M. 1998, AJ, 115, 1319
Dickinson, M., Giavalisco, M., & The GOODS Team. 2003, in The Mass of Galaxies at Low and High Redshift, ed. R. Bender & A. Renzini (Berlin: Springer), 324
Finkelstein, S. L., Rhoads, J. E., Malhotra, S., & Grogin, N. 2009, ApJ, 691, 465

Finkelstein, S. L., Rhoads, J. E., Malhotra, S., Grogin, N., & Wang, J. 2008, ApJ, 678, 655
Finkelstein, S. L., Rhoads, J. E., Malhotra, S., Pirzkal, N., & Wang, J. 2007, ApJ, 660, 1023
Fioc, M., & Rocca-Volmerange, B. 1997, A&A, 326, 950
Fioc, M., & Rocca-Volmerange, B. 1999, arXiv:astroph/9912179
Fujita, S. S., et al. 2003, AJ, 125, 13
Fynbo, J. U., Møller, P., & Thomson, B. 2001, A&A, 374, 443
Gawiser, E., et al. 2006, ApJ, 642, L13
Gawiser, E., et al. 2007, ApJ, 671, 278
Giavalisco, M., Steidel, C. C., Adelberger, K. L., Dickinson, M. E., Pettini, M., & Kellogg, M. 1998, ApJ, 503, 543
Giavalisco, M., Steidel, C. C., & Macchetto, F. D. 1996, ApJ, 470, 189
Gronwall, C., et al. 2007, ApJ, 667, 79
Guaita, L., et al. 2010, ApJ, 714, 255
Hansen, M., & Oh, S. P. 2006, MNRAS, 367, 979
Hu, E. M., Cowie, L. L., Capak, P., McMahon, R. G., Hayashino, T., & Komiyama, Y. 2004, AJ, 127, 563
Hu, E. M., Cowie, L. L., & McMahon, R. G. 1998, ApJ, 502, L99
Hu, E. M., & McMahon, R. G. 1996, Nature, 382, 231
Iwata, I., Ohta, K., Tamura, N., Akiyama, M., Aoki, K., Ando, M., Kiuchi, G., & Sawicki, M. 2007, MNRAS, 376, 1577
Iwata, I., Ohta, K., Tamura, N., Ando, M., Wada, S., Watanabe, C., Akiyama, M., & Aoki, K. 2003, PASJ, 55, 415
Iye, M., et al. 2004, PASJ, 56, 381
Iye, M., et al. 2006, Nature, 443, 186
Kajino, H., et al. 2009, ApJ, 704, 117
Kashikawa, N., et al. 2006, ApJ, 648, 7
Kennicutt, R. C. 1998, ARA&A, 36, 189
Kodaira, K., et al. 2003, PASJ, 55, L17
Kornei, K. A., Shapley, A. E., Erb, D. K., Steidel, C. C., Reddy, N. A., Pettini, M., & Bogosavljević, M. 2010, ApJ, 711, 693
Kudritzki, R.-P., et al. 2000, ApJ, 536, 19
Lai, K., Huang, J., Fazio, G., Cowie, L. L., Hu, E. M., & Kakazu, Y. 2007, ApJ, 655, 704
Lai, K., et al. 2008, ApJ, 674, 70
Lowenthal, J. D., et al. 1997, ApJ, 481, 673
Madau, P. 1995, ApJ, 441, 18
Malhotra, S., & Rhoads, J. E. 2002, ApJ, 565, L71
Malhotra, S., & Rhoads, J. E. 2004, ApJ, 617, L5
Miyazaki, S., et al. 2002, PASJ, 54, 833
Murayama, T., et al. 2007, ApJS, 172, 523
Neufeld, D. A. 1991, ApJ, 370, L85
Nilsson, K. K., Tapken, C., Møller, P., Freudling, W., Fynbo, J. P. U., Meisenheimer, K., Laursen, P., & Östlin, G. 2009, A&A, 498, 13
Nilsson, K. K., et al. 2007, A&A, 471, 71
Oke, J. B., & Gunn, J. E. 1983, ApJ, 266, 713
Ono, Y., et al. 2010, MNRAS, 402, 1580
Ota, K., et al. 2008, ApJ, 677, 12
Ouchi, M., et al. 2003, ApJ, 582, 60
Ouchi, M., et al. 2004, ApJ, 611, 660
Ouchi, M., et al. 2008, ApJS, 176, 301
Papovich, C., Dickinson, M., & Ferguson, H. C. 2001, ApJ, 559, 620
Papovich, C., et al. 2004, ApJ, 600, L111
Partridge, R. B., & Peebles, P. J. E. 1967, ApJ, 147, 868
Peng, C. Y., Ho, L. C., Impey, C. D., & Rix, H.-W. 2002, AJ, 124, 266
Pentericci, L., Grazian, A., Fontana, A., Salimbeni, S., Santini, P., de Santis, C., Gallozzi, S., & Giallongo, E. 2007, A&A, 471, 433
Pettini, M., Kellogg, M., Steidel, C. C., Dickinson, M., Adelberger, K. L., & Giavalisco, M. 1998, ApJ, 508, 539
Pirzkal, N., Malhotra, S., Rhoads, J. E., & Xu, C. 2007, ApJ, 667, 49
Reddy, N. A., Erb, D. K., Steidel, C. C., Shapley, A. E., Adelberger, K. L., & Pettini, M. 2005, ApJ, 633, 748
Reddy, N. A., Steidel, C. C., Erb, D. K., Shapley, A. E., & Pettini, M. 2006, ApJ, 653, 1004
Reddy, N. A., Steidel, C. C., Pettini, M., Adelberger, K. L., Shapley, A. E., Erb, D. K., & Dickinson, M. 2008, ApJS, 175, 48
Rhoads, J. E., & Malhotra, S. 2001, ApJ, 563, L5
Rhoads, J. E., Malhotra, S., Dey, A., Stern, D., Spinrad, H., & Jannuzi, B. T. 2000, ApJ, 545, L85
Rhoads, J. E., et al. 2004, ApJ, 611, 59
Salpeter, E. E. 1955, ApJ, 121, 161
Sawicki, M., & Thompson, D. 2005, ApJ, 635, 100
Sawicki, M., & Thompson, D. 2006, ApJ, 648, 299
Sawicki, M., & Yee, H. K. C. 1998, AJ, 115, 1329

Shapley, A. E., Steidel, C. C., Adelberger, K. L., Dickinson, M., & Giavalisco, M. 2003, ApJ, 588, 65

Shapley, A. E., Steidel, C. C., Adelberger, K. L., & Pettini, M. 2001, ApJ, 562, 95

Shimasaku, K., et al. 2003, ApJ, 586, L111

Shimasaku, K., et al. 2004, ApJ, 605, L93

Shimasaku, K., et al. 2006, PASJ, 58, 313

Shimizu, I., & Umemura, M. 2010, MNRAS, 406, 913

Steidel, C. C., Adelberger, K. L., Giavalisco, M., Dickinson, M., & Pettini, M. 1999, ApJ, 519, 1

Steidel, C. C., Adelberger, K. L., Shapley, A. E., Pettini, M., Dickinson, M., & Giavalisco, M. 2003, ApJ, 592, 728

Steidel, C. C., Giavalisco, M., Dickinson, M., & Adelberger, K. L. 1996, AJ, 112, 352

Taniguchi, Y., et al. 2005, PASJ, 57, 165

Venemans, B. P., et al. 2002, ApJ, 569, L11

Venemans, B. P., et al. 2004, A&A, 424, L17

Williams, R. E., et al. 1996, AJ, 112, 1335

Yabe, K., Ohta, K., Iwata, I., Sawicki, M., Tamura, N, Akiyama, M., & Aoki, K. 2009, ApJ, 693, 507

Yagi, M., Kashikawa, N., Sekiguchi, M., Doi, M., Yasuda, N., Shimasaku, K., & Okamura, S. 2002, AJ, 123, 66

Yoshida, M., et al. 2006, ApJ, 653, 988